AGU100 ADVANCING EARTH AND SPACE SCIENCE

JGR

Journal of Geophysical Research: Oceans

RESEARCH ARTICLE

10.1002/2017JC013548

Key Points:

- Summer 2010 sea ice loss in the Central Arctic enhanced mixed-layer warming, and consequently increasing oceanic heat flux and delaying ice growth
- Cool atmospheric conditions in summer 2013, driven by the large-scale circulation, reduced sea ice melt in the Central Arctic
- Oceanic heat flux during the freezing season in the Arctic outflow region was 2–4 W m^{-2}, accounting for 18–31% of basal ice energy balance

Correspondence to:
R. Lei,
leiruibo@pric.org.cn

Citation:
Lei, R., Cheng, B., Heil, P., Vihma, T., Wang, J., Ji, Q., et al. (2018). Seasonal and interannual variations of sea ice mass balance from the Central Arctic to the Greenland Sea. *Journal of Geophysical Research: Oceans*, *123*. https://doi.org/10.1002/2017JC013548

Received 12 OCT 2017
Accepted 12 MAR 2018
Accepted article online 23 MAR 2018

© 2018. American Geophysical Union. All Rights Reserved.

Seasonal and Interannual Variations of Sea Ice Mass Balance From the Central Arctic to the Greenland Sea

Ruibo Lei[1], Bin Cheng[2], Petra Heil[3,4], Timo Vihma[2], Jia Wang[5], Qing Ji[6], and Zhanhai Zhang[1]

[1]SOA Key Laboratory for Polar Science, Polar Research Institute of China, Shanghai, China, [2]Finnish Meteorological Institute, Helsinki, Finland, [3]Australian Antarctic Division, Hobart, Tasmania, Australia, [4]Antarctic Climate and Ecosystems Cooperative Research Centre, University of Tasmania, Hobart, Tasmania, Australia, [5]National Oceanic and Atmospheric Administration Great Lakes Environmental Research Laboratory, Ann Arbor, Michigan, USA, [6]Chinese Antarctic Center of Surveying and Mapping, Wuhan University, Wuhan, China

Abstract The seasonal evolution of sea ice mass balance between the Central Arctic and Fram Strait, as well as the underlying driving forces, remain largely unknown because of a lack of observations. In this study, two and three buoys were deployed in the Central Arctic during the summers of 2010 and 2012, respectively. It was established that basal ice growth commenced between mid-October and early December. Annual basal ice growth, ranging from 0.21 to 1.14 m, was determined mainly by initial ice thickness, air temperature, and oceanic heat flux during winter. An analytic thermodynamic model indicated that climate warming reduces the winter growth rate of thin ice more than for thick ice because of the weak thermal inertia of the former. Oceanic heat flux during the freezing season was 2–4 W m^{-2}, which accounted for 18–31% of the basal ice energy balance. We identified two mechanisms that modified the oceanic heat flux, i.e., solar energy absorbed by the upper ocean during summer, and interaction with warm waters south of Fram Strait; the latter resulted in basal ice melt, even in winter. In summer 2010, ice loss in the Central Arctic was considerable, which led to increased oceanic heat flux into winter and delayed ice growth. The Transpolar Drift Stream was relatively weak in summer 2013. This reduced sea ice advection out of the Arctic Ocean, and it restrained ice melt because of the cool atmospheric conditions, weakened albedo feedback, and relatively small oceanic heat flux in the north.

1. Introduction

Compared with the 1979–2010 climatology, the 2010–2013 Arctic summer sea ice extent were very low (Parkinson & Comiso, 2013; Stroeve et al., 2011; Wang et al., 2016); however, these summers experienced large interannual differences in both atmospheric and sea ice conditions. In 2010, because of a low ice volume at the beginning of the melt season (Stroeve et al., 2011) and a persistent large-scale cyclone over the Central Arctic during August, which strongly enhanced sea ice divergence (Kawaguchi et al., 2012), much of the ice in the Central Arctic was depleted during summer. An aerial survey showed ice concentration as low as 70–75% along the transect from 87.0°N to 89.5°N (Huang et al., 2016). In the Eurasian Basin, anomalous ice reduction resulted in larger oceanic heat flux in summer 2010 compared with the summers of 2002–2009 (Stanton et al., 2012). In September 2012, Arctic sea ice extent reached the 1979–2017 minimum (updated from Parkinson and Comiso (2013)). However, during that summer, ice concentration in most of the Central Arctic exceeded 95% because of the northward convergence of sea ice. In summer 2013, Arctic atmospheric conditions did not favor strong ice melt, resulting in a 33% increase of sea ice volume in autumn 2013 compared with the 2010–2012 average (Tilling et al., 2015). Atmospheric and oceanic conditions in summer are expected to have seasonally lagged effects on sea ice mass balance because of the large heat capacity of the ocean and sea ice. Comparison of the observed sea ice mass balance from summer to winter for various years will help improve understanding of the seasonally lagged thermodynamic effects.

The sea ice outflow from the Central Arctic to the Greenland Sea via the Transpolar Drift Stream (TDS) plays a significant role in the long-term changes of Arctic sea ice (Haller et al., 2014; Spreen et al., 2009). McPhee & Untersteiner (1982) were the first to estimate the oceanic heat flux into sea ice in the TDS region based on measurements of ice thickness and temperatures. Since then numerous sea ice mass balance buoys

(IMBs) have been deployed in the Central Arctic, with the bulk of the measurements acquired from late spring to early winter along the TDS (McPhee et al., 2003; Perovich et al., 2014; Wang et al., 2016). Nevertheless, measurements encompassing an entire ice growth season are rare. The loss of Arctic summer sea ice increases the solar energy absorbed by the ocean (Perovich et al., 2011) and enhances the oceanic heat flux available into winter. The quantification of this feedback within the TDS region, however, remains unresolved because of a lack of observations compared with other regions, e.g., the Beaufort Gyre.

The Arctic atmospheric Dipole Anomaly (DA) (Wang et al., 2009) and the difference in sea level pressure (SLP) between 84°N, 90°W and 84°N, 90°E (Central Arctic Index, CAI) (Vihma et al., 2012) can be used to characterize both the wind forcing in the TDS region and the outflow rate of sea ice from the Central Arctic to Fram Strait (Lei et al., 2016a). The sea ice pack within the Central Arctic is likely exposed to different atmospheric and oceanic forcing compared with ice in the marginal seas. Thus, the atmospheric circulation patterns inevitably influence the sea ice thermodynamics in the TDS region.

The aim of this study was to improve the understanding of the seasonal and interannual differences in the thermodynamic processes of sea ice in the TDS region. We used data collected by two and three ice-tethered buoys deployed in the summers of 2010 and 2012, respectively, during the Chinese National Arctic Research Expedition (CHINARE). The buoys covered three ice seasons (2010/2011, 2012/2013, and 2013/2014). In addition, remote-sensing-based products of sea ice concentration, atmospheric reanalysis data, and data from previous ice-tethered buoys were incorporated to identify the importance of the various processes that affect the seasonal evolution and interannual variability of the sea ice mass balance.

2. Data and Methods

2.1. CHINARE Buoy Data

Two types of buoy were used in this study. One was designed by the U.S. Cold Regions Research and Engineering Laboratory (CRREL), called IMB, and the other was designed by the Scottish Association for Marine Science, called the Snow and Ice Mass Balance Array (SIMBA). The CRREL IMB measures (a) the elevations of the snow (or ice) surface and the ice base using acoustic sounders (Campbell SR50A and Teledyne-Benthos PSA916, respectively), (b) vertical temperature profile from 1.0 m above the initial snow surface to 1.0–2.0 m below the initial ice bottom using a thermistor string with an interval of 0.1 m (Therm-X YSI-44033-BP), and (c) near-surface air temperature (Campbell 107) and pressure (Vaisala PTB210) (Richter-Menge et al., 2006). The SIMBA measures the air-ice-ocean temperature profile (Maxim Integrated DS28EA00) at higher vertical resolution (0.02 m) than the CRREL IMB (Jackson et al., 2013). A thermistor sensor (DS28EA00) together with a radiant shield was included with each SIMBA buoy to measure air temperature at 1.5 m above the snow surface. In addition, an acoustic underwater sounder (Teledyne-Benthos PSA916) was deployed at each SIMBA site to measure the position of the ice base. The sounder was deployed 1.5 m beneath the initial ice base through a hole (diameter: 0.10 m) using a polypropylene frame. This frame had an L-type hinged arm, which ensured the sounder could be positioned 0.20 m to the side of the borehole, to avoid a disturbance of the measurement by the borehole. The measurement accuracies of both types of buoy were 0.1 K for air, snow, and ice temperatures, and 0.01 m for the position of the ice base.

In August 2010, buoys A (CRREL IMB) and B (SIMBA) were deployed on the same floe 250 m apart, 270 km south of the North Pole (Table 1), from where they drifted within the TDS into Fram Strait (Figure 1). Data transmission from B ceased on 17 May 2011, while A continued its southward drift to the ice edge until 24 July 2011. In summer 2012, three SIMBA buoys (C, D, and E), each with a supplementary underwater sounder, were deployed in the Central Arctic. Unfortunately, buoy C suffered data transmission issues; hence, data were received only for the initial 4 months and for two short periods during the summers of 2013 and 2014. Buoy D transmitted continuously from September 2012 to February 2014, exceeding the operational lifespan of all IMBs deployed in the TDS. Eventually, buoys C and D drifted through Fram Strait onto the East Greenland Shelf. Buoy E operated from September 2012 to January 2013.

Our analyses used only those data obtained once the deployment holes had fully refrozen, i.e., 10 days after deployment for A, B, C, and E, and after 30 days for D, which had been deployed on substantially thicker ice than the other units. In the absence of direct measurements, the interface between air and snow (or ice) at B–E was estimated using the temperature profile, because the vertical temperature gradient (daily amplitude) in air was smaller (larger) than in snow and ice (Hoppmann et al., 2015; Provost et al., 2017). The

Table 1
Details of Buoy Operation and Sea Ice Mass Balance With Data for Buoy D Shown Separately for Each Ice Season

Buoy	A	B	C	D2012/2013	D2013/2014	E
Duration of data records	18 Aug 2010 to 24 Jul 2011	18 Aug 2010 to 17 May 2011	28 Aug–19 Dec 2012, 4 Jul–14 Aug 2013, and 19–24 May 2014	3 Sep 2012 to 16 Feb 2014		2 Sep 2012 to 25 Jan 2013
Deployment position	87.38°N, 172.26°W		86.80°N, 120.57°E	85.12°N, 147.40°E	N/A	84.13°N, 160.14°E
Ice thickness at deployment (m)	1.65	1.38	1.10	2.40	N/A	1.12
Basal freezing onset (ice thickness (m))	10 Nov 2010 (1.49)	9 Nov 2010 (1.14)	30 Oct 2012 (0.88)	10 Dec 2012 (2.12)	11 Nov 2013 (2.34)	15 Oct 2012 (0.72)
Max. ice thickness (m)	2.15	1.94	>2.02	2.71	2.55	N/A
Basal melt onset	25 Apr 2011	10 May 2011	N/A	21 Jun 2013	28 Jan 2014	N/A
Basal melt (m)	>0.45	N/A	N/A	0.37	N/A	N/A

accuracy for this estimation was about 0.02–0.04 m (Provost et al., 2017), i.e., slightly worse than the acoustic measurements (0.01 m).

2.2. Other Data

The data measured by IMB 2006D (which drifted from 87.56°N, 6.7°E to 83.92°N, 6.8°E from 1 June to 1 September 2007) were compared with those measured by CHINARE buoy D (which drifted from 88.31°N,

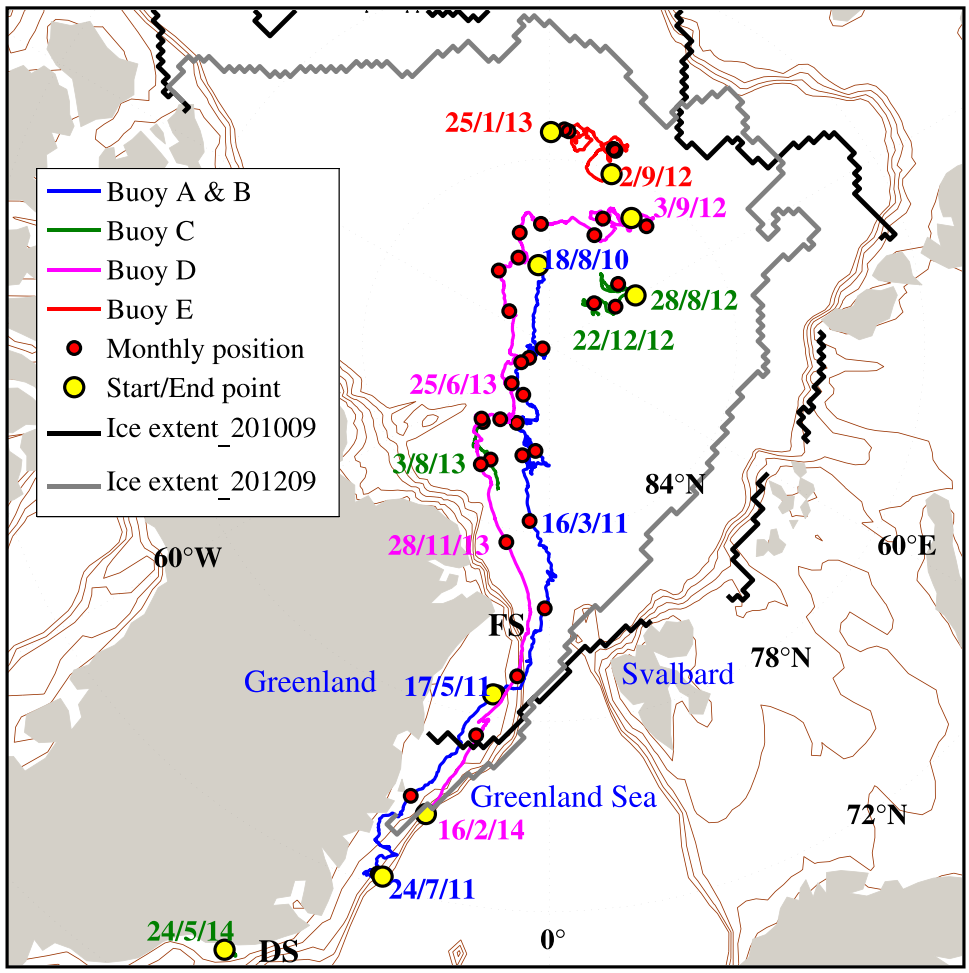

Figure 1. Trajectories of buoys A–E and their respective deployment, monthly, and terminal positions. Also shown are ice extents in September 2010 (black line) and 2012 (gray line), and isobaths from −1,000 to 0 m at a 250 m interval (thin brown lines). FS and DS denote Fram Strait and Denmark Strait, respectively.

130.83°W to 87.08°N, 35.36°W during the same months in 2013) because their respective positions were close to each other on 1 June, with distance of 430 km. The 2006D had been deployed north of the Laptev Sea as part of the Developing Arctic Modeling and Observing Capabilities for Long-term Environmental Studies (DAMOCLES) project. However, there are no historic IMB observations close to the location of buoy D during winter. In situ data were available from only one ice-tethered locating buoy deployed in 1993 (I2418), archived by the International Arctic Buoy Program (IABP). On 1 September, the positions of buoys I2418 (87.67°N, 63.49°E) and D (87.08°N, 35.36°W) were close, with distance of 446 km.

The 2 m air temperature (T2M) and incident solar radiation of the ERA-Interim reanalysis data (Dee et al., 2011) were used to characterize the atmospheric conditions along the trajectories of the buoys. We used the ERA-Interim product because, when compared with measurements from 449 weather stations north of 60°N, it was found to have smaller bias than other reanalysis products (Lindsay et al., 2014).

To clarify the feedback regime between summer sea ice conditions and winter sea ice growth, data from the Advanced Microwave Scanning Radiometer onboard EOS (AMSR-E) and its successor (AMSR2) (Spreen et al., 2008) were used to determine sea ice concentrations in the region of interest.

2.3. Energy Balance at the Ice Base

At the ice base, the energy balance can be described as follows (McPhee & Untersteiner, 1982):

$$F_c + F_l + F_s - F_w = 0, \tag{1}$$

where F_c is the conductive heat flux, F_l is the equivalent latent heat flux due to ice freezing or melting, F_s is the sensible heat flux due to ice cooling or warming, and F_w is the oceanic heat flux. The sign convention for heat fluxes is that upward, melting and warming fluxes are positive, and vice versa.

The conductive heat flux through the ice was estimated by

$$F_c = k_{si} \frac{\partial T_{si}}{\partial z_{si}}, \tag{2}$$

where k_{si} is the sea ice thermal conductivity and $(\partial T_{si}/\partial z_{si})$ is the vertical ice temperature gradient. Parameter k_{si} is a function of sea ice temperature and salinity (Untersteiner, 1961).

The latent and specific heat fluxes were calculated following Semtner (1976):

$$F_l = -\rho_{si} L_f \frac{\partial H_{si}}{\partial t} \tag{3}$$

and

$$F_s = \rho_{si} c_{si} \frac{\partial T_{si}}{\partial t}, \tag{4}$$

where L_f is the sea ice latent heat, $(\partial H_{si}/\partial t)$ is the ice growth rate, ρ_{si} is the sea ice density, c_{si} is the sea ice specific heat, and $(\partial T_{si}/\partial t)$ is the temporal rate of change in ice temperature. The latent and specific heats of sea ice are given as functions of its temperature and salinity (Untersteiner, 1961; Yen et al., 1991). Since the ice bottom layer contains a large brine fraction with small conductive heat flux, a reference layer is defined at 0.40–0.70 m above the ice base. F_c and F_s refer to the vertical gradient and temporal variation of ice temperature within this layer, respectively, and F_l refers to the basal ice growth or decay. To calculate k_{si} and c_{si}, we used the mean temperature of the reference layer. The ice density was set to 910 kg m^{-3} and the ice salinity was set to 8 psu within the reference layer, which are typical values of newly formed ice (e.g., Cox & Weeks, 1974). To calculate F_l, we also assumed an ice density of 910 kg m^{-3}. The value of L_f was derived as 0.215×10^6 J kg^{-1} by assuming an ice salinity of 12 psu and freezing temperature of −1.80°C. We chose a higher salinity for the calculation of F_l than for F_c and F_s, because F_l is related to the freshly formed ice layer at the bottom.

We limited the time series calculations of energy balance to the seasons of ice growth and early melt. This was because the vertical ice temperature would be isothermal during the fully developed melt season, which would then enhance gravity-driven desalination and give rise to large errors in the derived heat fluxes. Equation (1) was solved for F_w using a time step of 6 h. A 20 day sliding temporal window was used

to reduce the uncertainties in the measurements of ice temperature and basal growth. In the melt season, we assumed the energy balance only needed to balance the ice loss against oceanic heat flux, because both the conductive heat and specific heat fluxes were very close to zero. This hypothesis is acceptable if considering the temporal average (Ackley et al., 2015). Thus, we estimated the oceanic heat flux in the melt season using the temporal average ice melt rate.

Estimation errors associated with F_c, F_s, and F_l might propagate to F_w. Considering the possible ranges of sea ice and seawater physical parameters, with ice salinity of 4–12 psu for the reference layer and 9–15 psu for the ice bottom, ice density of 900–920 kg m^{-3}, seawater salinity of 30–34 psu, and the measurement accuracies of the thermistor string (0.1 K) and of the underwater sounder (0.01 m), the typical error for oceanic heat flux was estimated to be 1–2 W m^{-2} over a 20 day interval. This was considered acceptable for identifying seasonal variability. For detailed error analyses of the heat flux estimations, the reader is referred to Lei et al. (2014).

To assess the effect of oceanic heat flux on sea ice mass balance, we estimated ice growth using equation (1) by setting the oceanic heat flux to 0 W m^{-2} and scaling the conductive heat flux as inversely proportional to ice thickness as

$$F'_{ci} = F_{ci}\frac{H_{i-1}}{H'_{i-1}}, \tag{5}$$

where F_{ci} and F'_{ci} are the original and adjusted conductive heat fluxes at time i, respectively, and H_{i-1} and H'_{i-1} are the original and adjusted ice thicknesses at time $i-1$, respectively. A time step of 6 h was used here to compare the estimated ice growth with that observed.

2.4. Atmospheric Circulation Indices

To quantify the effect of the atmospheric circulation patterns regulating the sea ice thermodynamics within the TDS, we calculated the monthly Arctic Oscillation (AO) and DA indices, as well as the monthly CAI. The monthly SLP data of the NCEP reanalysis 2 north of 70°N were used to derive the empirical orthogonal function (EOF) modes, and the AO and DA were the first and second EOF modes (Wang et al., 2009). The CAI, which was defined as the difference in SLP between 84°N, 90°W and 84°N, 90°E, was calculated using the ERA-Interim reanalysis data according to Vihma et al. (2012).

2.5. Influence of Air Temperature Anomalies on Sea Ice Mass Balance

At the synoptic scale, the sea ice mass balance is driven by thermodynamic processes due to a range of external forcing factors. Here we used the most essential variable, i.e., the near-surface air temperature, to identify the influence of a changing climate on the sea ice mass balance. For all years from 1979 to 2014, the cumulative seasonal freezing degree day (FDD) and melt degree day (MDD) were calculated using the ERA-Interim T2M interpolated to the buoy sites. The FDD and MDD were defined as the time-integrated air temperature below the seawater freezing point (−1.8°C) and above the surface snow/ice melt point (0°C) during the freezing and melt seasons, respectively. Thus, the FDD (MDD) parameter largely reflects the atmospheric forcing on sea ice mass balance during the freezing (melt) season (Drobot et al., 2008; Petrich et al., 2012).

The revised Stefan analytical ice model (Leppäranta, 1993), which includes the contribution of oceanic heat flux, was applied to estimate sea ice growth for each freezing season of 1979–2014. This analytical model provides a first-order estimate of ice growth based on an assumption that the heat both released by freezing at the ice bottom and derived from the underlying ocean is conducted away through the ice in the form of a linear temperature gradient:

$$\frac{dH_{si}}{dt} = -\frac{k_{si}}{H_{si}\rho_{si}L_f}(T_s - T_f) + \frac{F_w}{\rho_{si}L_f}, \tag{6}$$

where T_s is the ice surface temperature and T_f is the ice freezing temperature (−1.80°C). We assumed a linear relationship between the T2M and the ice surface temperature, i.e., $T_s = \delta\cdot$T2M. The linear coefficient δ was determined daily using the ERA-Interim T2M and in situ T_s obtained during the operational year of each buoy. Given an initial ice thickness $H_{is} = H_0$ at $t = 0$, the analytical solution is

$$H_{si}=\sqrt{H_0^2+\alpha^2\mathrm{FDD}}-\frac{1}{\rho_{si}L_f}\int F_w dt, \tag{7}$$

where

$$\alpha=\sqrt{2k_{si}/\rho_{si}L_f}. \tag{8}$$

Here the FDD was determined using T_s. The L_f was also assumed as 0.215×10^6 J kg^{-1} and the ice density was set as 910 kg m^{-3}. Thus, we derived the daily freezing rate α as 0.037 m (°C^{-1} d^{-1})$^{0.5}$.

To identify the influence of anomalies in near-surface air temperature on the sea ice mass balance, we compared the sea ice growth derived using the revised Stefan model for a given year with the 1979–2014 mean.

3. Results

3.1. Local Atmospheric Conditions

In early September, near-surface air temperature decreased to below freezing point at all buoy sites (Figure 2). However, basal ice growth did not commence immediately because of the thermal inertia exerted by snow, ice, and brine pockets. Compared with other years, the autumn (September–November) of 2012 was warm, with mean near-surface air temperatures of −11.3°C, −11.1°C, and −10.5°C measured by buoys C, D, and E, respectively. In contrast, the autumns of 2010 and 2013 were colder, with mean near-surface air temperatures of −13.6°C and −15.2°C measured by buoys A/B and D, respectively. At sites A/B and D (2012/2013), the near-surface air temperature ranged between −15°C and −35°C during winter, which increased gradually from March to late May and then stabilized at around 0°C for summer. However, a gradual increase from as early as December 2013 was observed at site D, which coincided with the site having moved into the Greenland Sea.

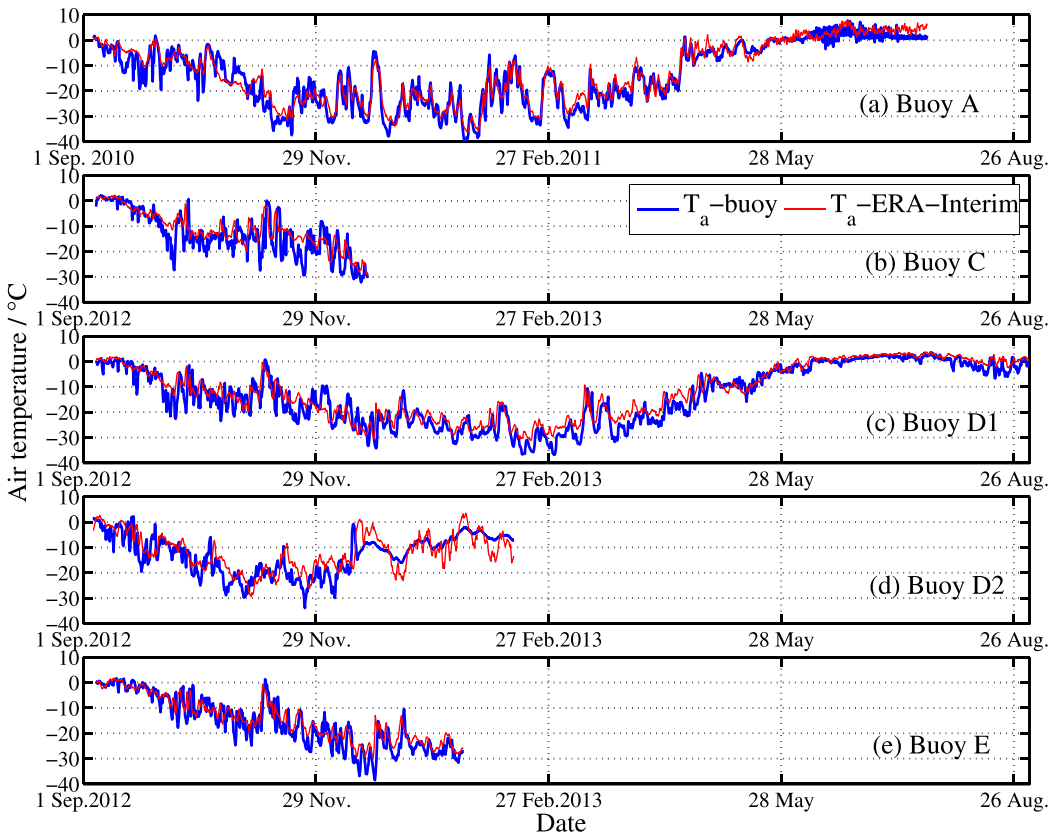

Figure 2. Near-surface air temperature measured by buoys and obtained from ERA-Interim T2M.

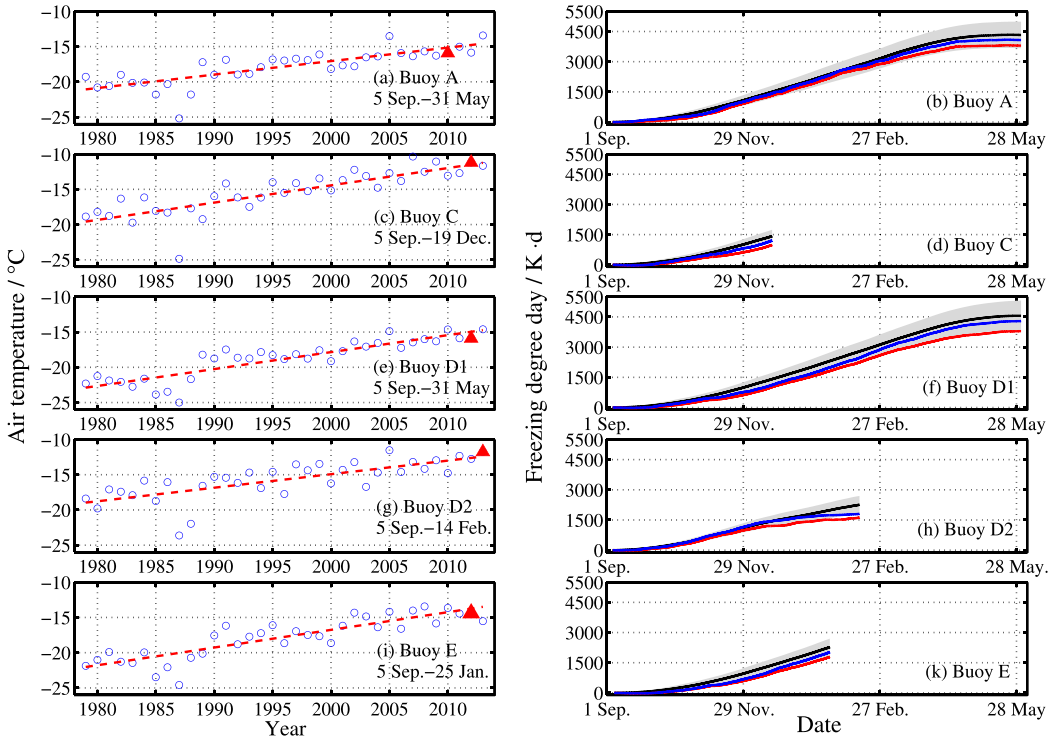

Figure 3. (left) Average near-surface air temperatures during the freezing season obtained from ERA-Interim T2M for the ice seasons of 1979–2014 and their linear trends (dashed red line), with red triangles denoting the operation years of the buoys. (right) Freezing degree days calculated at buoy sites using the average (±standard deviation) ERA-Interim T2M in 1979–2014 (black line and gray shading), ERA-Interim T2M obtained during the buoy operation years (red line), and near-surface air temperature measured by the buoys (blue line).

The ERA-Interim T2M values were somewhat higher than those measured by the buoys at 1.5 m above the snow surface (Figure 2), which is a characteristic that agrees with previous comparisons with in situ observations over the central Arctic sea ice (Jakobson et al., 2012). Generally, the discrepancy was within the range of 0.5–2.5 K; and the seasonal variability of ERA-Interim T2M data matched the observed data well at all sites. Therefore, we used the ERA-Interim T2M data to identify long-term changes in atmospheric conditions. As shown in Figure 3, during the freezing season, T2M had a significant increasing trend ($P < 0.01$) from 1979 to 2014 at all sites. During the buoy operational years, all sites acquired a lower FDD from September to May (or to the end of the buoy life) compared with the 1979–2014 climatology. The FDDs at sites A (2010/2011) and D (2012/2013) were comparable with each other, with values of 3,798 and 3,503 K·d, respectively.

Buoy D remained within the Central Arctic north of Greenland for the entire summer of 2013. The mean ERA-Interim T2M from June to August was 1.3°C in 2013 along the trajectory of D, which was colder than the 1979–2014 climatology (1.4°C) and in other years since 2010 (1.6–2.2°C). The AO index in summer 2013 was 1.29, much higher than the long-term mean of 0.02 ± 1.01 for 1979–2014. The positive AO induced a strong cyclonic circulation over the Arctic Ocean, which reduced not only the southward ice export from the Central Arctic (Ogi & Rigor, 2013) but also the poleward advection of relatively warm air (Wang et al., 2016).

3.2. Sea Ice Mass Balance

There was a remarkable loss of sea ice in the eastern sector of the Central Arctic in the summers of 2010 and 2013 (Figure 4). In the domain 85–88°N, 0–210°E, the average ice concentrations were 84% and 81% in August 2010 and 2013, respectively, each much lower than in other years between 2003 and 2013. We call this phenomenon the transpolar ice loss. In contrast to 2010 and 2013, the average ice concentration was 95% for August 2012, slightly larger than the 2003–2013 average (94%). This relatively high ice

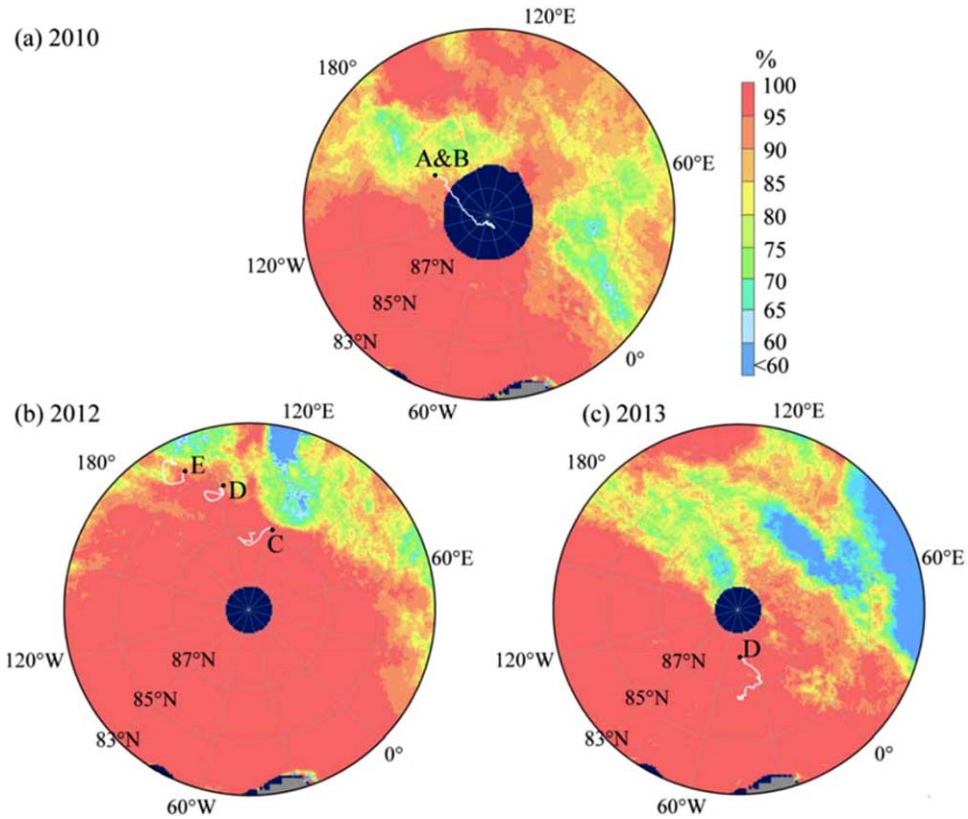

Figure 4. AMSR-E/AMSR2-derived sea ice concentrations for August 2010, 2012, and 2013. Trajectories (white lines) from sites of deployment (black dots) to (a) 30 September 2010 for buoys A and B, (b) 30 September 2012 for buoys C–E, and (c) from 1 August to 30 September 2013 for buoy D.

concentration can be attributed to anomalous southerly winds in the marginal seas from the Beaufort Sea to the Laptev Sea during summer 2012 (Wang et al., 2016).

Snow depth ranged from 0.2 to 0.3 m at the resumption of ice growth (Figure 5). Snow cover at A, B, and D accumulated from September to February, with the annual maximum snow depth ranging between 0.28 and 0.38 m. The initial ice thickness at B (1.14 m) was less than at A (1.49 m) at the onset of ice growth, explaining the higher basal growth rate observed at B throughout the growth season (Figures 5a and 5b). The average ice growth rates at A and B were 0.0040 and 0.0044 m d^{-1}, yielding total basal ice growths of 0.66 and 0.80 m, respectively. At the end of the 2012 melt season, C and E had relatively low ice thicknesses of 0.88 and 0.72 m, respectively (Figures 5c and 5e). Thus, basal ice growth resumed there early (30 and 15 October, respectively), even though the autumn near-surface air temperatures were slightly above those at A and B, where ice growth resumed in early November 2010. Ice thickness measured in summer 2013 confirmed that ice growth at C during the ice season of 2012/2013 exceeded 1.14 m (Figure 5c). This was nearly double that at D (0.59 m) during the same ice season (Figure 5d). Compared with the other sites, D had larger ice thicknesses of 2.12 and 2.34 m at the onset of freezing in 2012 and 2013, respectively. Thus, the new ice growth at site D started later than at the other sites, i.e., on 10 December 2012 and 11 November 2013, respectively. At D itself, much cooler conditions in summer-autumn 2013 resulted in the onset of ice growth occurring a month earlier in 2013 than in 2012. Nevertheless, in 2013/2014, ice growth at D (0.21 m) was only 36% of that in 2012/2013. This might be attributable largely to its more southerly position in 2013/2014. During the 2013/2014 ice growth season, the FDD at site D was 1,617 K·d, or only about 45% of that in 2012/2013.

Once south of 78°N, snow at site A had melted completely by 4 June 2011. Subsequently, surface ice melt reached 0.95 m by late July 2011 (Figure 5a), removing 44% of the ice thickness at melt onset. This surface ice melt was driven by the increasing availability of solar radiation as the site drifted southward into the

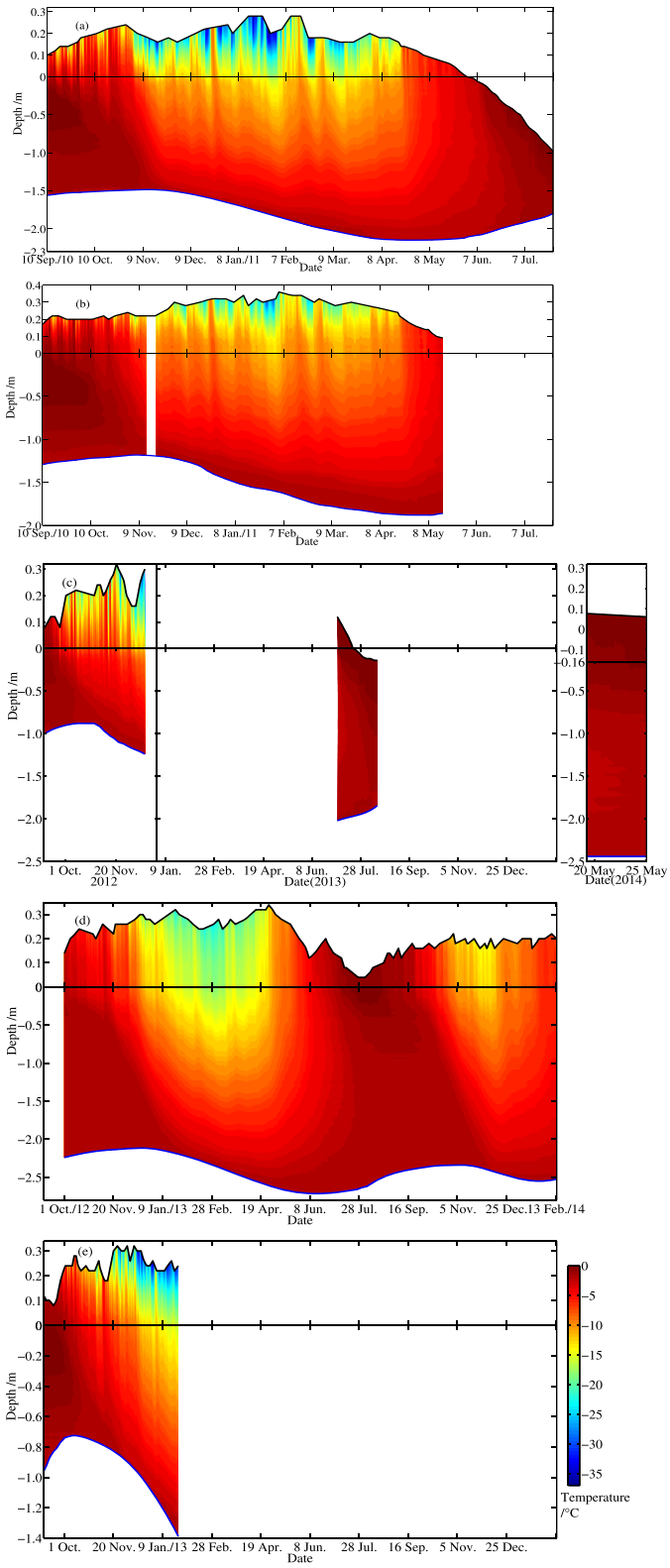

Figure 5. Snow and sea ice temperatures measured at buoys A–E (a–e). In the vertical axes, zero refers to the initial snow/ice interface. Black and blue lines represent the snow surface (ice surface when below the zero level) and the ice base, respectively. At site C, the snow/ice interface in summer 2014 was 0.16 m below that at deployment because of surface ice melt in summer 2013. Blanks denote data gaps.

Greenland Sea. In contrast, D experienced no surface ice melt during summer 2013 (Figure 5d) while transiting the pack ice zone (PIZ) in the Central Arctic. Its minimum snow depth (0.04 m) was recorded on 27 July 2013. The low surface melt rate at this site could be attributed to a combination of substantial snow accumulation between early March and mid-April 2013 and a relatively cool summer. The thicker snow cover at D by late April resulted in a negative feedback loop with higher albedo, preventing surface ablation during summer.

As A drifted onto the East Greenland Shelf during summer 2011, the basal ice melt was 0.45 m by late July, i.e., about half its surface ice melt (Figure 5a). The final recorded ice thickness was 0.72 m on 24 July 2011, i.e., 33% of ice thickness at melt onset. The basal ice melt at D (0.37 m) was less during summer 2013 (Figure 5d) than the ice growth (0.59 m) during the preceding freezing season (2012/2013), indicating positive annual mass balance. In the following ice season (2013/2014), basal ice melt at D started much earlier (28 January 2014) than in previous years. This early basal melt was likely due to its southern location (south of 77.34°N), where the site was exposed to large oceanic heat flux.

3.3. Basal Ice Energy Balance

Throughout the freezing season, the energy balance at the ice bottom showed that sensible heat flux was very small at all sites, whereas large amounts of heat were conducted upward away from the ice base. The seasonal change of the magnitude of the latent heat flux (F_L) agreed with that of the conductive heat flux (F_c) and opposed the oceanic heat flux (F_w). Therefore, sea ice growth was mainly characterized by F_c and F_w. The F_c contributed about 50% to the basal ice energy balance (Figure 6). During winter 2012/2013, the F_c at the thickest ice site D was relatively small (<15 W m^{-2}). This heat flux decreased gradually from halfway through the ice growth season because of increases in both ice thickness and near-surface air temperature. In particular, the F_c at D decreased to about 5 W m^{-2} by early February 2014 as the near-surface air temperature increased to about −5.6°C in the Greenland Sea.

The F_w revealed a large seasonal cycle. From late autumn, it decreased gradually to below 5 W m^{-2} by late December, after which it increased in response to the approaching summer or as a site exited the Central Arctic. The close agreement between the magnitude and seasonal evolution of F_w at A and B gives confidence in the performance of both measurement units (i.e., the CRREL IMB and the SIMBA supported by an underwater sounder). As shown in Figure 4, buoys A and B drifted within a region that had lower August ice concentration (<85%) than that surrounding buoys C (100%) and E (90–95%). In summer, an increase of

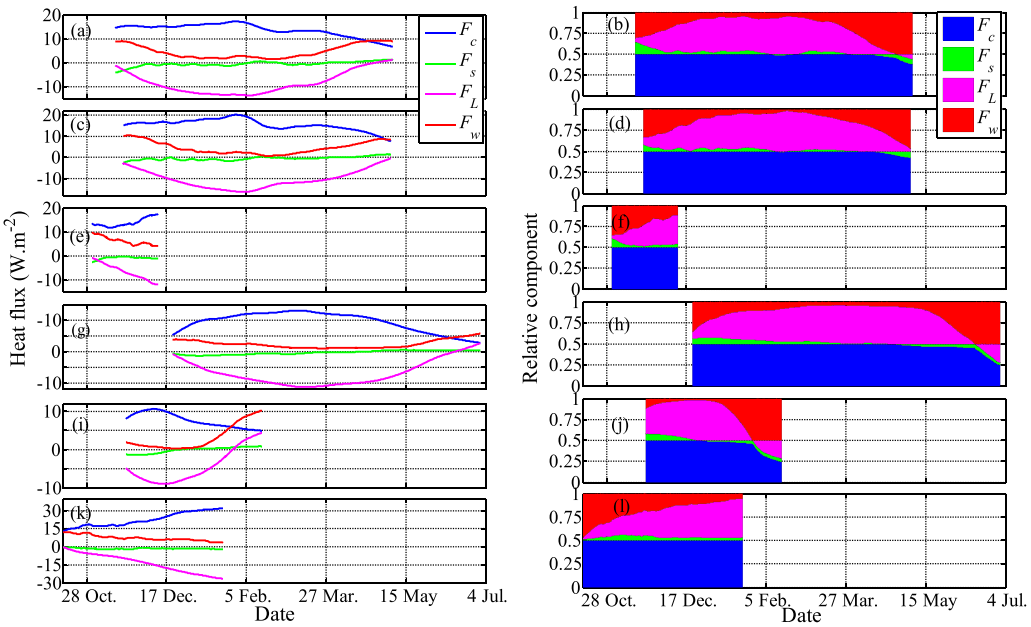

Figure 6. (left) Heat flux components and (right) their relative contributions to the sum of the flux magnitudes: (a and b) site A, (c and d) site B, (e and f) site C, (g and h) site D in 2012/2013, (i and j) site D in 2013/2014, and (k and l) site E.

10% in open-water area might translate into an increase of up to 7% in the absorption of solar radiation by the upper ocean (Lei et al., 2016b). Therefore, the November F_w (Figure 7) at A/B (8.3 W m^{-2}) slightly exceeded that at both C (6.7 W m^{-2}) and E (7.7 W m^{-2}). In November 2013, D was in the PIZ far from the marginal ice zone. Consequently, its F_w was merely 1.4 W m^{-2}. The F_w at A, B, and E showed a distinct decrease in winter, with monthly values less than 6.0, 4.5, and 2.0 W m^{-2} in December, January, and February, respectively. As A drifted from 84.3°N to 79.4°N during March–May 2011, F_w increased rapidly from 3.4 to 9.0 W m^{-2}. In contrast, in the Central Arctic, F_w at D remained below 2.0 W m^{-2} during spring 2013 and it only increased to 4.7 W m^{-2} by June 2013. The location of buoy D at the onset of basal ice melt in 2013 was 88.86°N, 75.42°W, where the lead fraction was very low, restricting the absorption of solar radiation by the upper ocean. The basal ice melt rate at D was 0.0026 m d^{-1} from 21 June to 11 November 2013, which was balanced by the oceanic heat flux of 7.7 W m^{-2}. In contrast, site A had a near double basal melt rate of 0.005 m d^{-1} from 25 April to 24 July 2011 as it drifted from 80.41°N to 72.31°N, which was balanced by the oceanic heat flux of 14.4 W m^{-2}. After summer, the F_w at D decreased gradually and it reached a small value of 0.5 W m^{-2} by December 2013, when D drifted into the PIZ north of Greenland. However, this heat flux increased rapidly to 3.5 and 9.2 W m^{-2} by January and February 2014, respectively. This is congruent with the ice floe being advected south of Fram Strait, where it would encounter the warm Atlantic water (Perovich et al., 1989). Close inspection of the drift trajectories of the buoys (A, B, and D), shown in Figure 1, suggests they were likely to encounter two branches of the West Spitsbergen Current, i.e., one branch that recirculates back into Fram Strait and the other that follows the western slope of the Yermak Plateau. In addition, heat advected from the open water is another mechanism that could adjust the oceanic heat flux south of Fram Strait (Provost et al., 2017). Both buoys A and D drifted close to the ice edge by the end of the measurement, where heat advected from the open water would enhance oceanic heat flux and accelerate ice basal decay.

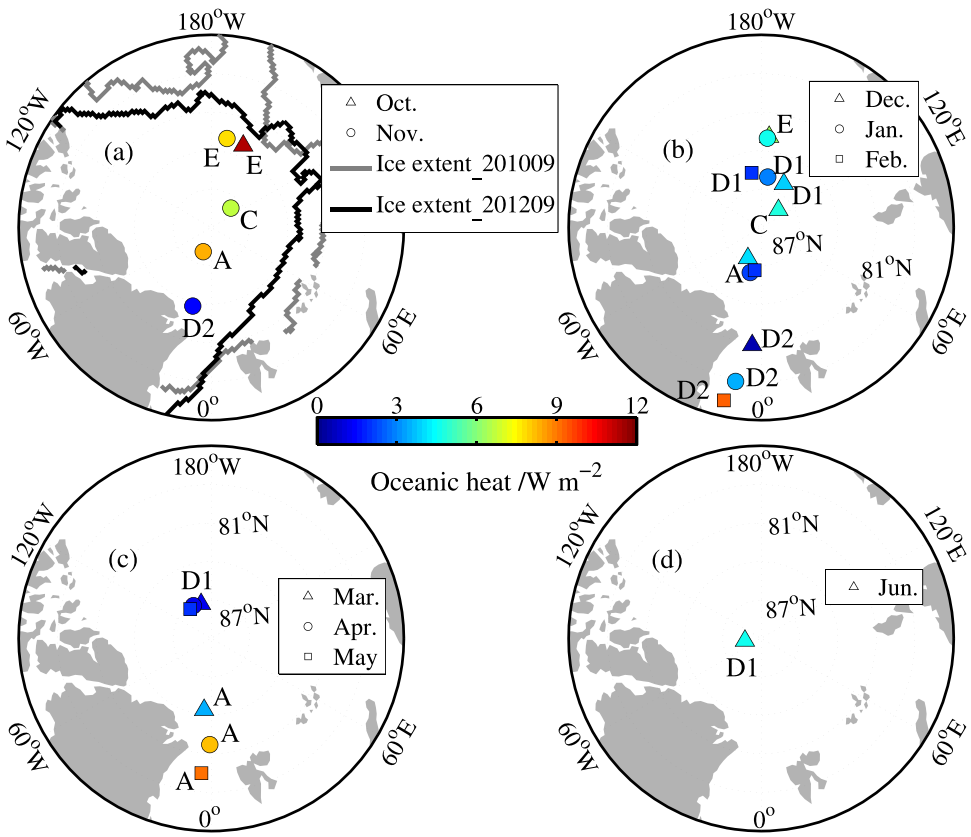

Figure 7. Monthly mean oceanic heat flux: (a) autumn, (b) winter, (c) spring, and (d) summer. Also shown in Figure 7a are the sea ice extents in September 2010 and 2012. D1 and D2 denote the location of D during the 2012/2013 and 2013/2014 ice seasons, respectively.

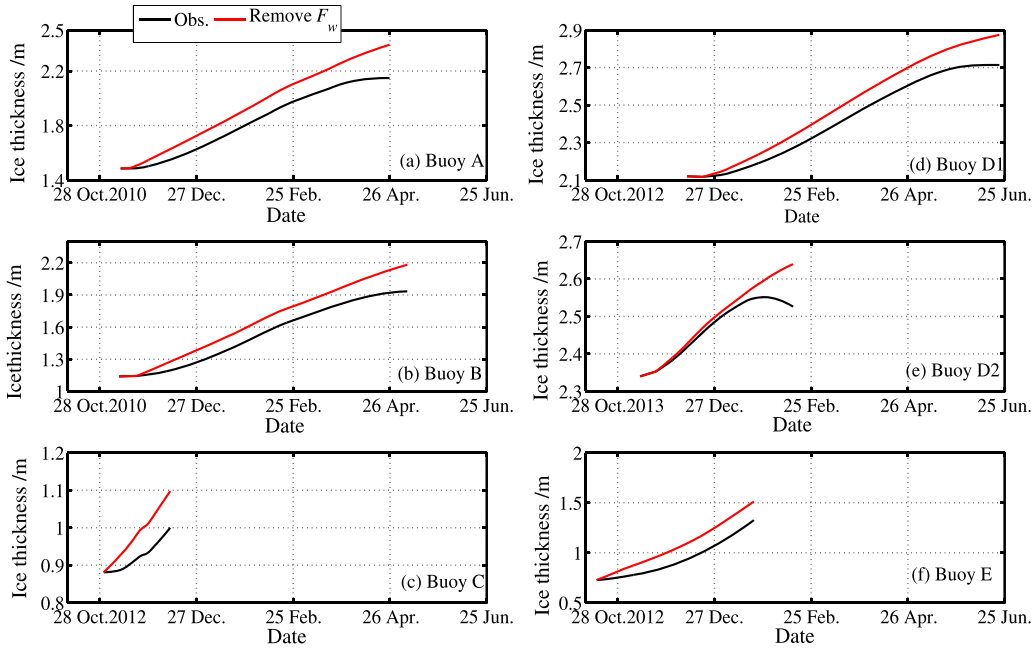

Figure 8. Sea ice thicknesses observed by the buoys and calculated by omitting oceanic heat flux.

From November 2010 to April 2011, the average F_w at A and B was 4.2 and 4.3 W m^{-2}, respectively, nearly double the long-term average value of 2.6 W m^{-2} obtained using upper-ocean hydrological measurements in the TDS region (Krishfield & Perovich, 2005). This difference was likely due to low summer ice concentrations encountered by A and B, which then resulted in large F_w during autumn. In contrast, the average F_w at D was relatively small during the freezing seasons of 2012/2013 (2.3 W m^{-2}) and 2013/2014 (1.6 W m^{-2}) because it drifted in the high-latitude PIZ from May to November 2013, where high ice concentrations restricted warming of the ocean by solar insolation.

Removing the oceanic forcing from the basal energy balance, the simulated ice growth increases by 0.24, 0.25, 0.16, and 0.11 m at sites A, B, D (2012/2013), and D (2013/2014), respectively (Figure 8). At site D (2013/2014), the oceanic heat flux was almost negligible prior to late December 2013, but from January 2014 onward, its effect on the simulated ice thickness increased rapidly. For the simulated result ignoring oceanic heat flux, the onset of basal ice melt at D still did not occur by mid-February 2014. Removal of oceanic heat flux caused a relative increase of 61% in ice growth, which was approximately twice the magnitude at buoys A (37%), B (31%), and D in 2012/2013 (27%). This confirms that oceanic forcing was a dominating factor driving the basal ice melt at site D during winter 2013/2014.

3.4. Impact of Atmospheric Circulation Patterns on Sea Ice Mass Balance

In summer (June–August) 2013, both the DA index (−0.46) and CAI (−0.4 hPa) were much lower than the 1979–2014 climatological means (Figures 9e and 9f). In contrast, in 2007, both the DA index (2.03) and CAI (3.8 hPa) were much higher than the climatological means. These patterns suggest that atmospheric forcing within the TDS region encouraged greater southward ice advection in summer 2007 than in summer 2013. The near-surface wind speeds along the TDS were, in fact, weak in summer 2007, but the wind direction was aligned persistently with the TDS, favoring accelerated ice export toward Fram Strait (Vihma et al., 2008). From 1 June to 1 September 2013, the CHINARE buoy D drifted from 88.31°N to 87.08°N. During the same period in 2007, the 2006D drifted more directly toward the south from 87.56°N to 83.92°N, with 220 km southward displacement during August alone (Figure 9a).

Based on the measurements of surface melt, the equivalent ice surface melt (H_{eq}) was estimated as 0.30 m at site 2006D in summer 2007, i.e., about 5 times the value at site D (0.06 m) in summer 2013. The H_{eq} includes the ice equivalent snow melt and surface ice melt (Perovich et al., 2014), and it was determined by setting the snow density and ice density to 300 and 910 kg m^{-3}, respectively. Summer 2013 was relatively cold in contrast to the comparatively warm summer in 2007. Consequently, along the trajectory of buoy D,

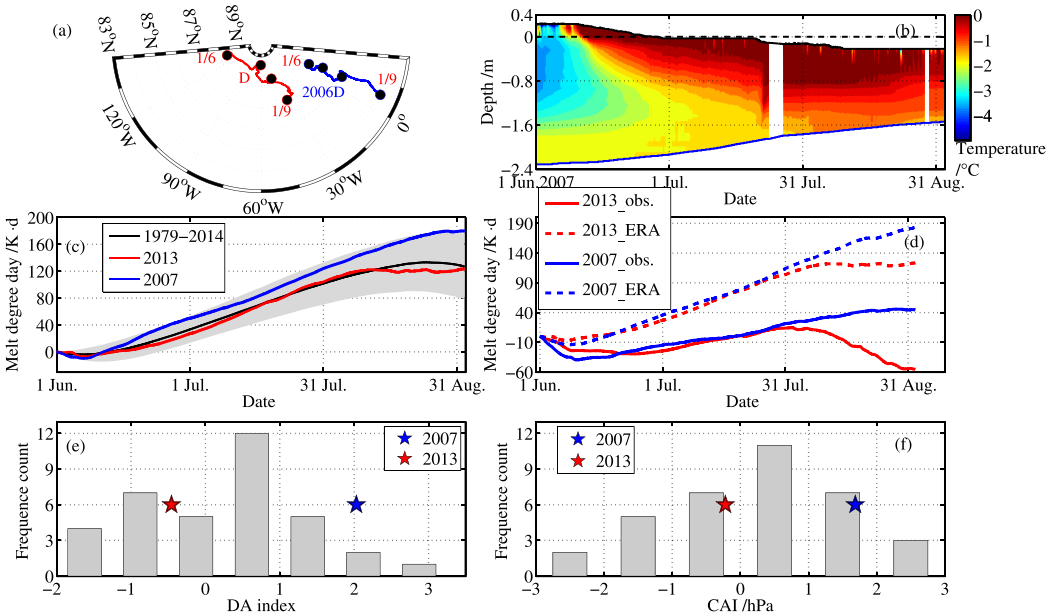

Figure 9. (a) Trajectories from 1 June to 1 September of buoy 2006D in 2007 and buoy D in 2013 and their monthly positions (black circles). (b) Snow and sea ice temperatures measured by buoy 2006D with black and blue lines representing the snow surface (ice surface when below the zero level) and the ice base, respectively. (c) Melt degree days accumulated along the trajectory of D in 2007 and 2013, and for the 1979–2014 climatology. (d) Melt degree days accumulated along the trajectories of D (2013) and 2006D (2007) determined using the buoy measurements and ERA-Interim data. (e and f) Frequency distributions of DA indices and CAIs in the summers of 1979–2014; also shown are the values in the summers of 2007 and 2013.

the MDD in 2013 (2007) was slightly smaller (much larger) than the 1979–2014 climatology (Figure 9c). The MDD obtained along the trajectory of buoy 2006D in summer 2007 was remarkably larger than that obtained along the trajectory of buoy D in summer 2013. The discrepancy increased rapidly after 1 August as 2006D drifted rapidly southward (Figure 9d). When air temperature rises above 0°C, the sensible and longwave heat fluxes might turn toward the snow surface, which could either increase the temperature of the snow or produce melting (Persson et al., 2002). The positive MDD accumulated in summer 2007 at site 2006D could effectively promote surface melt. In contrast, the negative MDD accumulated in summer 2013 at site D implies that the near-surface air temperature was mostly not beneficial to surface melt.

During the summer, solar radiation plays a more important role in relation to surface melting than both sensible heat and longwave fluxes (Persson et al., 2002; Vihma et al., 2008). The effect of solar radiation was estimated using ERA-Interim 12 h average incident solar radiaion and an albedo parameterization based on the surface status (Perovich et al., 2002). At site 2006D, the albedo at the beginning of summer 2007 was presumed to be 0.81 (the value of wet snow), which decreased linearly to 0.71 when the snow cover melted completely, and then decreased linearly to 0.65 (the value between bare ice and ponded ice) by 31 August 2007 as the 0.22 m surface ice melted (Figure 10a). At site D, the albedo at the beginning of summer 2013 was also presumed to be 0.81, which increased linearly to 0.85 (the value of dry snow) by 23 June 2013 because of the intermittent accumulation of snow. It then decreased linearly to 0.75 (the value between wet snow and bare ice) by 27 July 2013 because of melting of the snow. Finally, it increased linearly to 0.85 by 31 August 2013 because of snow accumulation (Figure 10c). The integrated total downward solar radiative flux between 1 June and 31 August 2013 along the trajectory of buoy D was 87.7 MJ m^{-2} (or 10.1%) larger than along the trajectory of buoy 2006D, because buoy D encounted longer periods of daylight in the north. However, the integrated total net solar radiative flux at the surface along the trajectory of 2006D was 52.3 MJ m^{-2} (or 28.3%) larger than along the trajectory of buoy D. During summer, although the duration of solar illumination dominates the cumulative incident solar energy available for the Arctic region (Vihma et al., 2008), the effect of the albedo feedback likely surpasses the total available solar energy and combines with the warm air temperature in summer 2007 to cause strong surface melting.

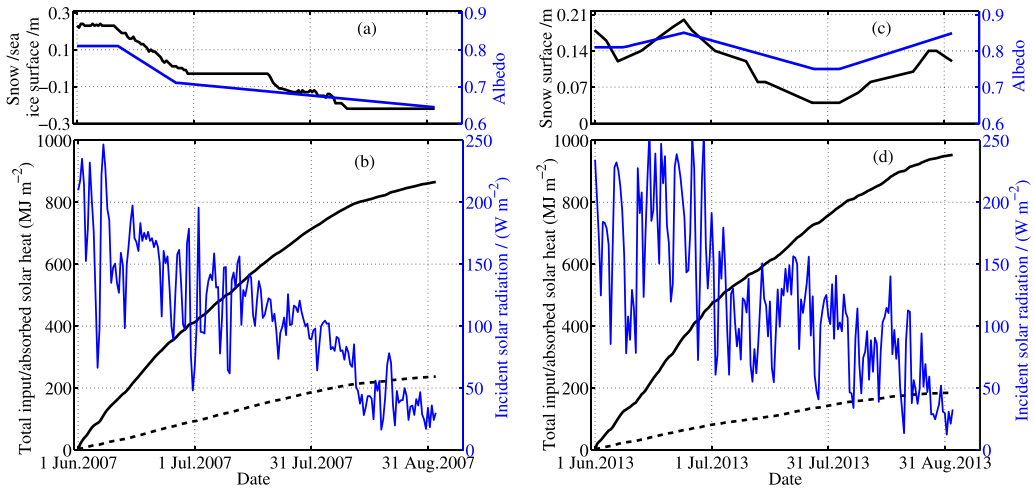

Figure 10. Snow or sea ice surface (black line) measured by buoys (a) 2006D and (c) D, and the albedo parameterization (blue line), and time series of cumulative incident (black solid line) and absorbed solar energy (black dashed line) by the surface, as well as the 12 h average incident solar radiaion (blue line) at sites (b) 2006D and (d) D.

The more southern location of 2006D would also have exposed this site to greater oceanic heat flux. The basal ice melt was 0.77 m at 2006D in summer 2007, about 3 times that observed at D (0.26 m) in summer 2013. The corresponding oceanic heat fluxes needed to balance the ice basal decay were 24.8 and 8.4 W m^{-2} at 2006D in summer 2007 and at D in summer 2013, respectively. This comparison demonstrates the critical effect of atmospheric circulation on sea ice motion and mass balance during the melt season in the Arctic outflow region.

A remarkable change in the Arctic atmospheric circulation pattern occurred in autumn-winter 2013. The September–December mean values of the DA index and CAI were 0.81 and 3.7 hPa, respectively (Figures 11c and 11d). Accordingly, buoy D drifted rapidly southward from 87.08°N, 35.36°W to 78.67°N, 7.51°W

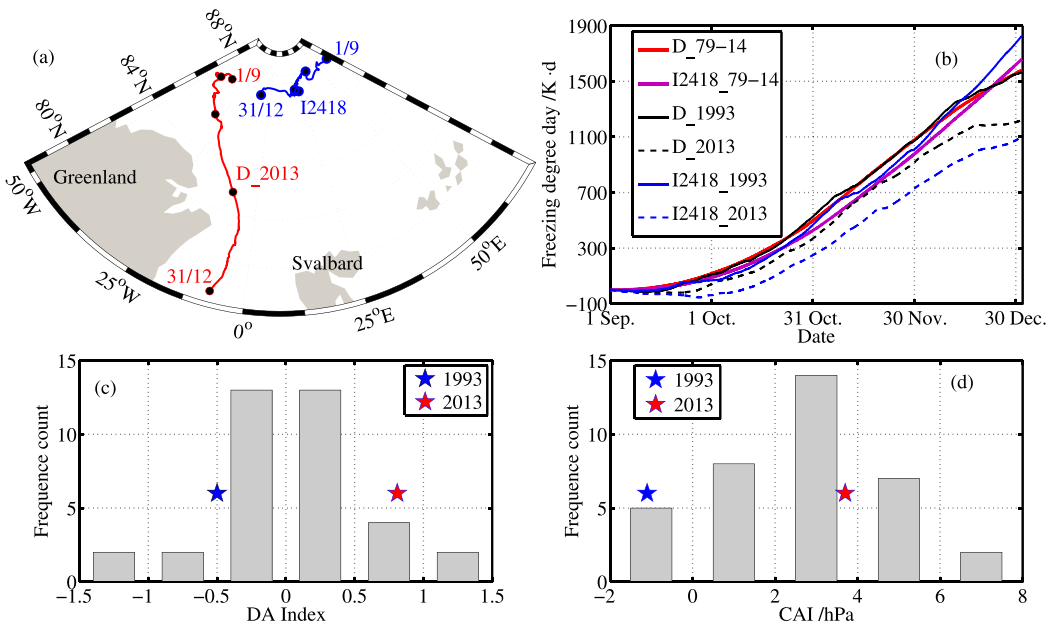

Figure 11. (a) Trajectories from 1 September to 31 December of buoy D in 2013 (red line) and buoy I2418 in 1993 (blue line) with monthly positions (black circles). (b) Freezing degree days accumulated along the trajectories of D and I2418 from 1 September to 31 December in 1993 and 2013, and for the 1979–2014 climatology. (c and d) Frequency distributions of average DA indices and CAIs during September–December 1979–2014; also shown are the values in 1993 and 2013.

(Figure 11a). The atmospheric circulation pattern in September–December 1993 was obviously different from that in 2013. The monthly average DA index and CAI during September–December 1993 were −0.5 and −1.1 hPa, respectively. Both were relatively low compared with the 1979–2014 climatology (Figures 11c and 11d). Accordingly, buoy I2418 drifted slowly southeastward from 87.67°N, 63.49°E to 87.09°N, 8.14°W in this period. The southward displacement was only about 65 km over 4 months, or about 7% of the distance traveled by buoy D during the same time in 2013. However, the FDD climatology for 1979–2014 was almost the same along the trajectories of the two buoys (Figure 11b). In 1993, the FDD along the trajectory of I2418 was comparable with that along the trajectory of D until mid-December, after which the FDD increased more rapidly along the former trajectory. Nevertheless, in 2013, the FDD along the trajectory of I2418 was always smaller than along the trajectory of D. This is related to the cold surface conditions in the northward and eastward offshore regions of Greenland. The near-surface air temperature north of Greenland was lower than or equal to the region near the North Pole. This demonstrates how the large zonal thermal gradient from Greenland to the Barents Sea affects the sea ice mass balance in the Arctic outflow region.

3.5. Impact of Air Temperature Anomaly on Sea Ice Mass Balance

Air temperatures resampled along our buoy trajectories during 1979–2014 were the coldest in 1987 (Figure 2), which would have influenced the ice seasons of both 1986/1987 and 1987/1988. Along the trajectories of A–E, the long-term changes in T2M were 1.8 ± 0.3 and 1.3 ± 0.5°C decade^{-1} for 1979–2014 and 1989–2014, respectively. To assess the influence of anomalies in near-surface air temperature on sea ice mass balance, we compared the observed ice thicknesses from the buoys with the estimated values for 1979–2014 and 1989–2014 using the analytical ice model (equation (6)). Because of the observed Arctic climate warming, recent ice growth was less than the 1989–2014 climatology at all sites, with the exception of site D in 2012/2013 because of the relatively cold spring and summer experienced in 2013 (Figure 12). The climatological ice growth of 1989–2014 was smaller than that of 1979–2014 at all sites, with the longer time series encapsulating the cold seasons of 1986/1987 and 1987/1988. At sites with buoy observations over the complete growth season of A, B, D1 (2012/2013), and D2 (2013/2014), the discrepancies in ice thicknesses by the end of the growth season between the observed values and the 1979–2014 climatology ranged from −0.09 m at D1 (2012/2013) to −0.21 m at D2 (2013/2014). The sensitivity to the anomaly of air temperature was more evident for thin ice in comparison with thick ice because of the weak thermal inertia of the

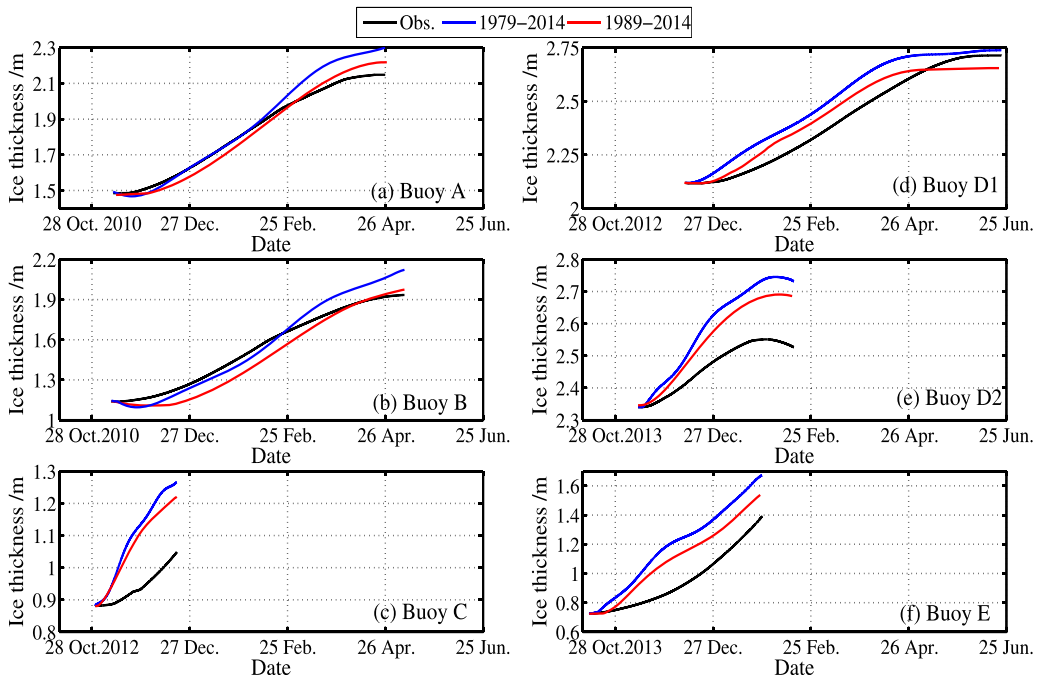

Figure 12. Sea ice thicknesses observed by the buoys and calculated using the average ERA-Interim T2M over 1979–2014 and 1989–2014.

former. During the same season (2012/2013), the differences between the observed ice thicknesses and the 1979–2014 climatology were much larger at C and E with thinner ice thicknesses than at D.

4. Discussion and Conclusions

Our IMB data cover the 2010/2011, 2012/2013, and 2013/2014 ice seasons. We analyzed the IMB data together with other supporting data to identify the parameters that dominate the sea ice mass balance in the Arctic outflow region. Our results showed that several parameters drive the sea ice mass balance: ice conditions in the preceding summer, as well as snow accumulation, near-surface air temperature, and geographical position at times of ice growth. These factors act to determine the thermal inertia, surface heat balance, conductive heat flux through the ice cover, and the oceanic heat flux available during the ice growth season.

The large-scale pattern of sea ice distribution with a clear sea ice loss across the eastern sector of the Central Arctic during summer 2010 gave rise to increased autumn oceanic heat flux, as experienced by sites A and B. Although the Arctic sea ice extent reached a record minimum in summer 2012, ice conditions in the interior of the pack ice zone were dominated by convergence, limiting the absorption of solar radiation by the upper ocean. Summer sea ice loss in the central Arctic similar to 2010 was observed in 2013. However, low melt rates were observed for both snow and ice at site D during that summer. This was attributed to the following factors: (a) D was trapped in the pack ice zone, (b) summer 2013 was cold compared with the recent record associated with the positive AO, and (c) the oceanic heat flux encountered by D was the smallest in our data record. Our in situ observations provide crucial insight into why Arctic sea ice extent averaged for September 2013 increased by 1.72×10^6 km^2 (or 32%) compared with the record low of September 2012.

The basal seasonal ice growth at buoys A–D, which ranged from 0.21 to 1.14 m was inversely proportional to the initial ice thickness at freezing onset ($R^2 = 0.805$, $P < 0.05$). If oceanic heat flux was omitted, then the range of ice growth would increase by 0.04 m at D (2013/2014) and by 0.22 m at B. This highlights the importance of oceanic heat flux on the basal energy balance. For the ice drifting to the south of Fram Strait during summer, surface melt was comparable with or larger than the basal melt due to the higher air temperature and increased solar radiation at lower latitudes. In the regions south of Fram Strait, basal ice decay occurred even in winter because of the relatively high oceanic heat flux.

The influence of oceanic heat flux on sea ice mass balance weakened from autumn to winter, and strengthened again in spring. The average oceanic heat flux during the ice growth season ranged from 1.6 to 4.4 W·m^{-2}, accounting for 34–58% of that obtained in the region of Transpolar Drift Stream during summer (Stanton et al., 2012). Two regimes contribute to the change in oceanic heat flux under the ice. Generally, the upper ocean warms in the summer mainly via the absorption of solar radiation through leads. The warming of the upper ocean leads to the formation of near-surface temperature maxima below the halocline (Jackson et al., 2010). The heat within the near-surface temperature maxima is then released upward because of an upwelling event or the seasonal deterioration of the halocline, which acts to reduce basal ice growth in winter (Jackson et al., 2012). In the region south of Fram Strait, the increase in oceanic heat flux was attributed to the encounter with Atlantic warm waters and the horizontal convection of heat from the open water.

The complexities of seasonal and spatial changes, together with their modulation by regional changes in ice concentration and oceanic stratification, complicate the parameterization of oceanic heat flux for numerical simulations of sea ice thermodynamics. It is difficult to differentiate the spatial and temporal variations of oceanic heat flux using Lagrangian measurements from only a few ice-tethered buoys. A sustained basin-scale network of Arctic buoys is needed to address this challenge. Because sea ice growth rate is strongly dependent on initial ice thickness, a distributed network for sea ice mass balance measurements at the floe scale over sufficient representative points is very necessary to characterize spatial heterogeneity. Uncertainty in the salinity of surface seawater is the dominant error source in the estimation of oceanic heat flux via the energy balance method. Seawater salinity changes regionally and temporally in the Arctic outflow region (Koenig et al., 2016). Thus, we recommend installation of a conductivity sensor in the IMB (e.g., Ackley et al., 2015). Furthermore, combining the deployments of IMBs and ice-tethered ocean profilers

could help quantify the thermodynamic interactions between sea ice and the ocean mixed layer (e.g., Koenig et al., 2016).

The positive anomalies of the DA index and CAI favor faster southward drift of sea ice in the region of Transpolar Drift Stream. Compared with the Central Arctic, ice advected into the Greenland Sea and to its south might generally experience warmer atmospheric and oceanic conditions, which would then promote summer melting and reduce winter freezing. The higher value of MDDs in summer 2007 created surface melting that triggered the positive albedo feedback that lead to greater surface melting at site 2006D compared with D in summer 2013. The surface melt (basal melt) at site 2006D during summer 2007 was about 5 (3) times that at buoy D in summer 2013. Thus, the strengthened Transpolar Drift Stream was a crucial factor that contributed to the recorded minimum Arctic sea ice extent of September 2007 by increased advection of sea ice out of the Arctic Ocean. However, this sequence does not always hold because it also depends on basin-scale zonal thermal gradients. For example, site D, which was advected southward into the region to the north of Greenland during autumn-winter 2013, did experience surface air temperatures as cold as the ice that remained close to the North Pole. The atmospheric thermal gradients from north to south and between the north of Greenland and the north of the Barents Sea drive the large spatial variability of atmospheric forcing for sea ice mass balance in the Arctic outflow region.

The ice growth at all our sites during 2010–2013 was less than the long-term average ice growth for 1979–2014 derived using the revised Stefan model. Arctic warming affects thin ice more profoundly than thick ice because it reduces winter growth rates of thin ice more than those of thick ice. Thus, we infer that the thermodynamic processes of Arctic sea ice will become increasingly sensitive to climate warming as the sea ice thins further, which will then contribute directly to increased loss in Arctic sea ice volume.

Acknowledgments
Passive microwave ice concentrations were provided by the University of Bremen. The T2M data from the ERA-Interim reanalysis have been obtained from the ECMWF. The IABP is acknowledged for providing data for buoy I2418 (http://iabp.apl.washington.edu), and the DAMOCLES project is recognized for supplying data for IMB 2006D (https://imb.erdc.dren.mil). This work was supported by grants from the National Key Research and Development Program (2016YFC14003) and National Natural Science Foundation of China (41476170/41722605). B.C. and T.V. were funded by the Academy of Finland (283101). P.H. was supported by the Antarctic Climate and Ecosystems CRC Program and AAS grant 4301. J.W. was supported by the NOAA CPO Office of Arctic Research. Buoy data are available at the Chinese National Arctic and Antarctic Data Center (http://www.chinare.org.cn/difDetailPublic/?id=8721).

References

Ackley, S. F., Xie, H., & Tichenor, E. A. (2015). Ocean heat flux under Antarctic sea ice in the Bellingshausen and Amundsen Seas: Two case studies. *Annals of Glaciology*, *56*(69), 200–210. https://doi.org/10.3189/2015AoG69A890

Cox, G. F. N., & Weeks, W. F. (1974). Salinity variations in sea ice. *Journal of Glaciology*, *13*(67), 109–120.

Dee, D. P., Uppala, S. M., Simmons, A. J., Berrisford, P., Poli, P., Kobayashi, S., et al. (2011). The ERA-Interim reanalysis: Configuration and performance of the data assimilation system. *Quarterly Journal of the Royal Meteorological Society*, *137*, 553–597. https://doi.org/10.1002/qj.828

Drobot, S., Stroeve, J., Maslanik, J., Emery, W., Fowler, C., & Kay, J. (2008). Evolution of the 2007–2008 Arctic sea ice cover and prospects for a new record in 2008. *Geophysical Research Letters*, *35*, L19501. https://doi.org/10.1029/2008GL035316

Haller, M., Brümmer, B., & Müller, G. (2014). Atmosphere-ice forcing in the transpolar drift stream: Results from the DAMOCLES ice-buoy campaigns 2007–2009. *The Cryosphere*, *8*, 275–288.

Hoppmann, M., Nicolaus, M., Hunkeler, P. A., Heil, P., Behrens, L.-K., König-Langlo, G., et al. (2015). Seasonal evolution of an ice-shelf influenced fast-ice regime, derived from an autonomous thermistor chain. *Journal of Geophysical Research: Oceans*, *120*, 1703–1724. https://doi.org/10.1002/2014JC010327

Huang, W., Lu, P., Lei, R., Xie, H., & Li, Z. (2016). Melt pond distribution and geometry in high Arctic sea ice derived from aerial investigations. *Annals of Glaciology*, *57*, 105–118. https://doi.org/10.1017/aog.2016.30

Jackson, J. M., Carmack, E. C., McLaughlin, F. A., Allen, S. E., & Ingram, R. G. (2010). Identification, characterization and change of the near surface temperature maximum in the Canada Basin, 1993 − 2008. *Journal of Geophysical Research*, *115*, C05021. https://doi.org/10.1029/2009JC005265

Jackson, J. M., Williams, W. J., & Carmack, E. C. (2012). Winter sea-ice melt in the Canada Basin, Arctic Ocean. *Geophysical Research Letters*, *39*, L03603. https://doi.org/10.1029/2011GL050219

Jackson, K., Wilkinson, J., Maksym, T., Meldrum, D., Beckers, J., Haas, C., et al. (2013). A novel and low cost sea ice mass balance buoy. *Journal of Atmospheric and Oceanic Technology*, *30*(11), 13825. https://doi.org/10.1175/JTECH-D-13-00058.1

Jakobson, E., Vihma, T., Palo, T., Jakobson, L., Keernik, H., & Jaagus, J. (2012). Validation of atmospheric reanalyses over the central Arctic Ocean. *Geophysical Research Letters*, *39*, L10802. https://doi.org/10.1029/2012GL051591

Kawaguchi, Y., Hutchings, J. K., Kikuchi, T., Morison, J. H., & Krishfield, R. A. (2012). Anomalous sea-ice reduction in the Eurasian Basin of the Arctic Ocean during summer 2010. *Polar Science*, *6*, 39–53.

Koenig, Z., Provost, C., Villacieros-Robineau, N., Sennechael, N., & Meyer, A. (2016). Winter ocean-ice interactions under thin sea ice observed by IAOOS platforms during N-ICE2015: Salty surface mixed layer and active basal melt. *Journal of Geophysical Research: Oceans*, *121*, 7898–7916. https://doi.org/10.1002/2016JC012195

Krishfield, R. A., & Perovich, D. K. (2005). Spatial and temporal variability of oceanic heat flux to the Arctic ice pack. *Journal of Geophysical Research*, *110*, C07021. https://doi.org/10.1029/2004JC002293

Lei, R., Heil, P., Wang, J., Zhang, Z., Li, Q., & Li, N. (2016a). Characterization of sea-ice kinematic in the Arctic outflow region using buoy data. *Polar Research*, *35*, 22658. http://doi.org/10.3402/polar.v35.22658

Lei, R., Li, N., Heil, P., Cheng, B., Zhang, Z., & Sun, B. (2014). Multiyear sea-ice thermal regimes and oceanic heat flux derived from an ice mass balance buoy in the Arctic Ocean. *Journal of Geophysical Research: Oceans*, *119*, 537–547. https://doi.org/10.1002/2012JC008731

Lei, R., Tian-Kunze, X., Leppäranta, M., Wang, J., Kaleschke, L., & Zhang, Z. (2016b). Changes in summer sea ice, albedo, and portioning of surface solar radiation in the Pacific sector of Arctic Ocean during 1982–2009. *Journal of Geophysical Research: Oceans*, *121*, 5470–5486. https://doi.org/10.1002/2016JC011831

Leppäranta, M. (1993). A review of analytical sea-ice growth models. *Atmosphere-Ocean*, *31*(1), 123–138.

Lindsay, R., Wensnahan, M., Schweiger, A., & Zhang, J. (2014). Evaluation of seven different atmospheric reanalysis products in the Arctic. *Journal of Climate*, *27*(7), 2588–2606.

McPhee, M. G., Kikuchi, T., Morison, J. H., & Stanton, T. P. (2003). Ocean-to-ice heat flux at the North Pole environmental observatory. *Geophysical Research Letters*, *30*(24), 2274. https://doi.org/10.1029/2003GL018580

McPhee, M. G., & Untersteiner, N. (1982). Using sea ice to measure vertical heat flux in the ocean. *Journal of Geophysical Research*, *87*(C3), 2071–2074. https://doi.org/10.1029/JC087iC03p02071

Ogi, M., & Rigor, I. G. (2013). Trends in Arctic sea ice and the role of atmospheric circulation. *Atmospheric Science Letters*, *14*, 97–101.

Parkinson, C. L., & Comiso, J. C. (2013). On the 2012 record low Arctic sea ice cover: Combined impact of preconditioning and an August storm. *Geophysical Research Letters*, *40*, 1356–1361. https://doi.org/10.1002/grl.50349

Perovich, D., Richter-Menge, J., Polashenski, C., Elder, B., Arbetter, T., & Brennick, O. (2014). Sea ice mass balance observations from the North Pole Environmental Observatory. *Geophysical Research Letters*, *41*, 2019–2025. https://doi.org/10.1002/2014GL059356

Perovich, D. K., Grenfell, T. C., Light, B., & Hobbs, P. V. (2002). Seasonal evolution of the albedo of multiyear Arctic sea ice. *Journal of Geophysical Research*, *107*(C10), 8044. https://doi.org/10.1029/2000JC000438

Perovich, D. K., Jones, K. F., Light, B., Eicken, H., Markus, T., Stroeve, J., et al. (2011). Solar partitioning in a changing Arctic sea-ice cover. *Annals of Glaciology*, *52*(57), 192–196.

Perovich, D. K., Tucker, W. B. III, & Krishfield, R. A. (1989). Oceanic heat flux in the Fram Strait measured by a drifting buoy. *Geophysical Research Letters*, *16*(9), 995–998. https://doi.org/10.1029/GL016i009p00995

Persson, P. O. G., Fairall, C. W., Andreas, E. L., Guest, P. S., & Perovich, D. K. (2002). Measurements near the Atmospheric Surface Flux Group tower at SHEBA: Near-surface conditions and surface energy budget. *Journal of Geophysical Research*, *107*(C10), 8045. https://doi.org/10.1029/2000JC000705

Petrich, C., Eicken, H., Zhang, J., Krieger, J., Fukamachi, Y., & Ohshima, K. I. (2012). Coastal landfast sea ice decay and breakup in northern Alaska: Key processes and seasonal prediction. *Journal of Geophysical Research*, *117*, C02003. https://doi.org/10.1029/2011JC007339

Provost, C., Sennéchael, N., Miguet, J., Itkin, P., Rösel, A., Koenig, Z., et al. (2017). Observations of flooding and snow-ice formation in a thinner Arctic sea-ice regime during the N-ICE2015 campaign: Influence of basal ice melt and storms. *Journal of Geophysical Research: Oceans*, *122*, 7115–7134. https://doi.org/10.1002/2016JC012011

Richter-Menge, J. A., Perovich, D. K., Elder, B. C., Claffey, K., Rigor, I., & Ortmeyer, M. (2006). Ice mass balance buoys: A tool for measuring and attributing changes in the thickness of the Arctic sea-ice cover. *Annals of Glaciology*, *44*, 205–210.

Semtner, A. J. (1976). A model for the thermodynamic growth of sea ice in numerical investigations climate. *Journal of Physical Oceanography*, *6*, 379–389.

Spreen, G., Kaleschke, L., & Heygster, G. (2008). Sea ice remote sensing using AMSR-E 89 GHz channels. *Journal of Geophysical Research*, *113*, C02S03. https://doi.org/10.1029/2005JC003384

Spreen, G., Kern, S., Stammer, D., & Hansen, E. (2009). Fram Strait sea ice volume export estimated between 2003 and 2008 from satellite data. *Geophysical Research Letters*, *36*, L19502. https://doi.org/10.1029/2009GL039591

Stanton, T. P., Shaw, W. J., & Hutchings, J. K. (2012). Observational study of relationships between incoming radiation, open water fraction, and ocean-to-ice heat flux in the Transpolar Drift: 2002–2010. *Journal of Geophysical Research*, *117*, C07005. https://doi.org/10.1029/2011JC007871

Stroeve, J. C., Maslanik, J., Serreze, M. C., Rigor, I., Meier, W., & Fowler, C. (2011). Sea ice response to an extreme negative phase of the Arctic Oscillation during winter 2009/2010. *Geophysical Research Letters*, *38*, L02502. https://doi.org/10.1029/2010GL045662

Tilling, R. L., Ridout, A., Shepherd, A., & Wingham, D. J. (2015). Increased Arctic sea ice volume after anomalously low melting in 2013. *Nature Geoscience*, *8*, 643–646.

Untersteiner, N. (1961). On the mass and heat budget of Arctic sea ice. *Archiv für Meteorologie, Geophysik und Bioklimatologie, Serie A*, *12*, 151–182. https://doi.org/10.1007/BF02247491

Vihma, T., Jaagus, J., Jakobson, E., & Palo, T. (2008). Meteorological conditions in the Arctic Ocean in spring and summer 2007 as recorded on the drifting ice station Tara. *Geophysical Research Letters*, *35*, L18706. https://doi.org/10.1029/2008GL034681

Vihma, T., Tisler, P., & Uotila, P. (2012). Atmospheric forcing on the drift of Arctic sea ice in 1989–2009. *Geophysical Research Letters*, *39*, L02501. https://doi.org/10.1029/2011GL050118

Wang, C., Granskog, M. A., Hudson, S. R., Gerland, S., Pavlov, A. K., Perovich, D. K., et al. (2016). Atmospheric conditions in the central Arctic Ocean through the melt seasons of 2012 and 2013: Impact on surface conditions and solar energy deposition into the ice-ocean system. *Journal of Geophysical Research*, *121*, 1043–1058. https://doi.org/10.1002/2015JD023712

Wang, J., Zhang, J., Watanabe, E., Mizobata, K., Ikeda, M., Walsh, J. E., et al. (2009). Is the Dipole Anomaly a major driver to record lows in the Arctic sea ice extent? *Geophysical Research Letters*, *36*, L05706. https://doi.org/10.1029/2008GL036706

Yen, Y. C., Cheng, K. C., & Fukusako, S. (1991). Review of intrinsic thermophysical properties of snow, ice, sea ice, and frost. In Zarling, J. P. & Faussett, S. L. (Eds.), *Proceedings 3rd international symposium on cold regions heat transfer, Fairbanks, AK* (pp. 187–218). Fairbanks, AK: University of Alaska.